Check for updates

Delaney Park Geotechnical Array Dynamic Properties Inferred from the Magnitude 7.1 2018 Anchorage, Alaska, Earthquake Sequence

Erol Kalkan, A.M.ASCE[1]; Weiping Wen[2]; and YeongAe Heo, A.M.ASCE[3]

Downloaded from ascelibrary.org by Harbin Institute of Technology on 10/24/20. Copyright ASCE. For personal use only; all rights reserved.

Abstract: We used waveforms from the 2018 M_W 7.1 Anchorage earthquake and six selected aftershocks, ranging from M_W 4.2 to 5.7, to quantify site properties including shear-wave velocity profile, predominant frequencies, borehole amplification, soil-damping ratio, and shear modulus at Delaney Park in downtown Anchorage, Alaska. The waveforms were recorded by surface and six borehole (up to 61-m depth) three-component accelerometers. The deconvolution of the waveforms at various borehole depths on horizontal sensors with respect to the corresponding waveform at the surface provides incident and reflected traveling waves within the soil column. The shear-wave velocities determined from these events are consistent, and generally agree well with the in situ measurements. The borehole amplification based on surface-to-borehole traditional standard spectral ratio (SSR) and surface-to-borehole response spectral ratio (RSR) and cross-spectral ratio (c-SSR) were also evaluated. Based on c-SSR, we computed the borehole amplification as 4.8 at 1.35 Hz (0.74 s), close to the predominant frequency of the soil column. **DOI: 10.1061/(ASCE)GT.1943-5606.0002413.** *© 2020 American Society of Civil Engineers.*

Author keywords: Borehole amplification; Downhole array; Wave propagation; Interferometry; Deconvolution; Shear-wave velocity; Spectral analysis; Bootlegger Cove Formation; Monte Carlo simulation; Uncertainty analysis.

Introduction

Anchorage, Alaska, lies within one of the most active tectonic environments, and thus has been subjected to frequent seismic activity. The city is built on the edge of a deep sedimentary basin at the foot of Chugach Mountain range. The basin is more than 1 km thick in the western part of Anchorage, and reaches 7-km depth at a point about 150 km southwest of the city (Hartman et al. 1974). Shear-wave velocities, measured at 36 sites (Nath et al. 1997) in the basin, indicate that most of the city is on sediments that fall in National Earthquake Hazards Reduction Program (NEHRP) Site Categories C ($360 < V_{S30} < 760$ m/s; V_{S30} = average shear-wave velocity of upper 30 m of crust) and D ($180 < V_{S30} < 360$ m/s) (Boore 2004). The existence of low-velocity sediments overlying metamorphic bedrock can produce strong seismic waves (Borcherdt 1970). The Great Alaska earthquake (also known as the Prince William Sound earthquake) with M_W 9.2 on March 27, 1964, damaged the city, creating extensive liquefaction, landslides, and subsidence as large as 3 m in the downtown area (Updike and Carpenter 1986; Lade et al. 1988), and moved much of coastal Alaska seaward at least 80 m due to ground failures.

In 2003, the USGS established a seven-level downhole array of three-component accelerometers at Delaney Park (DPK) in downtown Anchorage in order to measure sediment response to earthquake shaking and to provide input wave-field data for soil–structure interaction studies of a nearby 20-story steel moment frame building (Atwood Building), which was also instrumented (Yang et al. 2004). Fig. 1 depicts this downhole array and Atwood Building in the background. The deepest downhole sensors are located at 61 m depth within the soil layer.

The 2018 M_W 7.1 Anchorage earthquake and its aftershocks were recorded at the DPK array. These recordings provide an excellent opportunity to extract the site properties and compare them with those from the earlier studies. The waveforms from the main shock and its six selected aftershocks, ranging from M_W 4.2 to 5.7, are rich enough in low-frequency content that the borehole amplifications can be computed at low frequencies.

First, we applied deconvolution interferometry to the waveforms from these seven events in order to compute the shear-wave velocity profile. The deconvolution interferometry provides a simple model of wave propagation by considering correlation of motions at different observation points (e.g., Aki 1957; Claerbout 1968; Trampert et al. 1993; Lobkis and Weaver 2001; Roux and Fink 2003; Schuster et al. 2004; Bakulin and Calvert 2006; Snieder et al. 2006). It also yields more repeatable and higher resolution wave fields than does cross-correlation interferometry (Nakata and Snieder 2012; Wen and Kalkan 2017). Our approach is similar but we identified incident and reflected deconvolved waves and used time reversal to determine the site properties. Although deconvolution and cross-correlation interferometry are interrelated, we preferred the deconvolution interferometry for this study because the effects of the external source have been removed in the latter approach (Snieder and Safak 2006; Rahmani and Todorovska 2013). Second, we estimated predominant frequencies of the DPK array by computing surface-to-borehole standard spectral ratio (SSR). Third, we computed borehole amplification based on SSR, surface-to-borehole cross-spectral ratio (c-SSR), and

[1]CEO, QuakeLogic Inc., 1849 San Esteban C., Roseville, CA 95747. ORCID: https://orcid.org/0000-0002-9138-9407. Email: erol@quakelogic.net

[2]Associate Professor, Key Lab of Structures Dynamic Behavior and Control of the Ministry of Education, Harbin Institute of Technology, Harbin 150090, China (corresponding author). Email: wenweiping@hit.edu.cn

[3]Assistant Professor, Dept. of Civil and Environmental Engineering, Case Western Reserve Univ., 10900 Euclid Ave., Cleveland, OH 44106. ORCID: https://orcid.org/0000-0003-4905-9997. Email: yxh549@case.edu

Note. This manuscript was submitted on November 26, 2019; approved on July 15, 2020; published online on October 24, 2020. Discussion period open until March 24, 2021; separate discussions must be submitted for individual papers. This paper is part of the ***Journal of Geotechnical and Geoenvironmental Engineering***, © ASCE, ISSN 1090-0241.

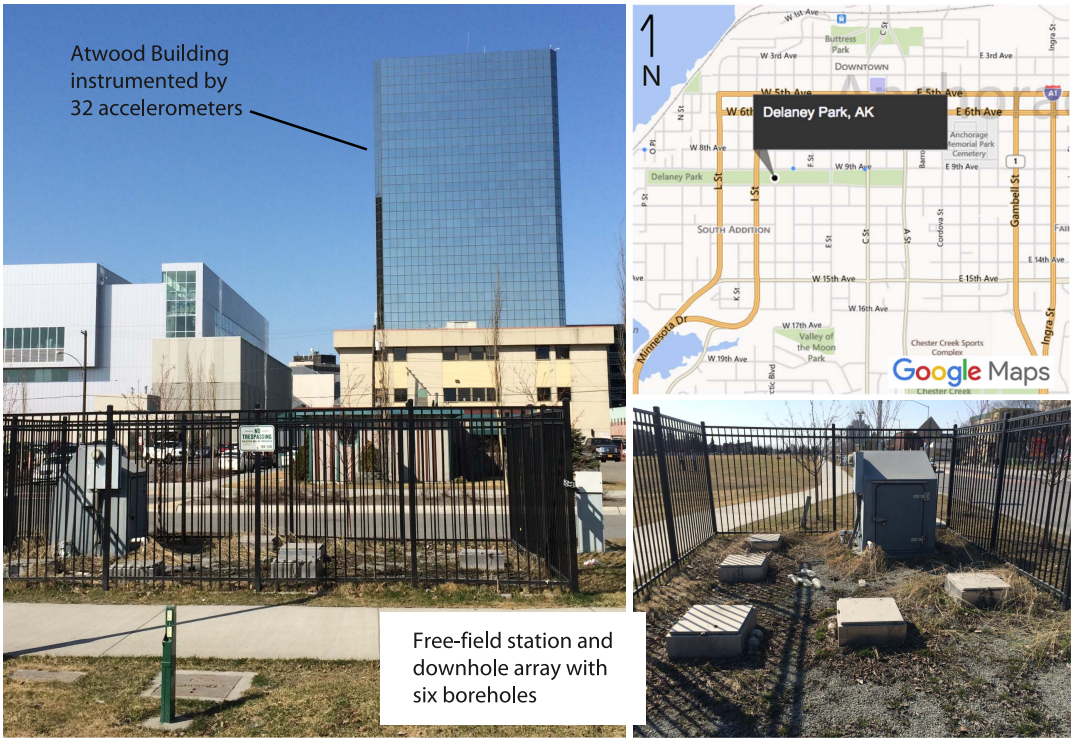

Fig. 1. DPK borehole array in downtown Anchorage, Alaska. The Atwood Building (20-story steel moment frame) in the background (165 m away from DPK array) is also instrumented. The map insert shows the location of Delaney Park. (Map data © 2020 Google, images by Erol Kalkan.)

surface-to-borehole response spectral ratio (RSR). Finally, we calculated soil-damping ratio and shear modulus, which are important parameters for geotechnical applications.

Tectonic Setting

The Anchorage area is located in the upper Cook Inlet region. Cook Inlet is situated in a tectonic forearc basin that is bounded to the west by the Bruin Bay–Castle Mountain fault system and to the east by the Knik fault along the west front of the Chugach Mountains as depicted in Fig. 2 (Lade et al. 1988). Most of the regional seismicity can be attributed to underthrusting along the Benioff zone (within ~150 km of Anchorage) of the plate boundary megathrust (Li et al. 2013). Large historical earthquakes have ruptured much of the length of this megathrust (Wong et al. 2010). The Benioff zone (shown by the thick dashed line) dips to the northwest beneath the Cook Inlet region (Fogelman et al. 1978). Smart et al. (1996) suggests that dextral slip on the Castle Mountain fault follows a complex fault array in the Matanuska Valley and strike-slip duplex systems in the northern Chugach Mountains. There is some evidence suggesting that the Castle Mountain fault systems may be active, and capable of propagating moderate-size earthquakes (Bruhn 1978; Lahr et al. 1986). The Castle Mountain fault approaches to within about 40 km of the city. Each year earthquakes with moment magnitudes above 4.5 are felt in Anchorage as a result of this tectonic setting.

Site and Instrumentation

The DPK array is located in the northwestern part of downtown Anchorage (Fig. 1). The geological section at the site consists of glacial outwash, overlying the Bootlegger Cove Formation (BCF) and glacial till deposited in a late Pleistocene glaciomarine-glaciodeltaic environment (14,000–18,000 years ago) (Ulery and Updike 1983). The alluvium and glacial outwash contain clay and silt, commonly stratified, deposited by glacial meltwater. These surficial mud layers of soft estuarine silts overlie an approximately 35-m-thick glacioestuarine deposit of stiff to hard clays with interbedded lenses of silt and sand; this glacioestuarine material is known locally as the BCF. Underlying the BCF is a glaciofluvial deposit from the early Naptowne glaciation (Updike and Carpenter 1986) consisting mainly of dense to very dense sands and gravels with interbedded layers of hard clay (Finno and Zapata-Medina 2014).

The DPK array has been deployed to sample the ground motions within the BCF as well as above and below it. The array consists of one surface and six borehole triaxial accelerometers located at 4.6, 10.7, 18.3, 30.5, 45.4, and 61 m deep, and oriented to cardinal directions as marked in Fig. 3. The deepest borehole sensor is located in a glacial till formation with shear-wave velocity $(V_S) > 650$ m/s. These borehole depths do not correspond to the depth of the boundary of soil layers. The accelerometers in boreholes (episensors) are connected to four six-channel, 24-bit data loggers (Quanterra-330, Kinemetrics, Pasadena, California).

Thornley et al. (2019) performed downhole velocity profiling measurements to derive the shear-wave velocity (V_S) profile (Fig. 4) at the DPK. This figure shows that the V_S increases initially within the glacial outwash at shallower depths, and then decreases within the deeper BCF. The depth of the higher-velocity alluvium and outwash materials is estimated to be approximately 10 m where the lower velocity structure of the BCF starts to appear. Nath et al. (1997) and Yang et al. (2008) also provided the V_S profile from inversion of data at a nearby site, about 200 m away. However, Thornley et al. (2019) found that those profiles are not suitable for the DPK array after evaluating the transfer functions of records between the instruments.

Downloaded from ascelibrary.org by Harbin Institute of Technology on 10/24/20. Copyright ASCE. For personal use only; all rights reserved.

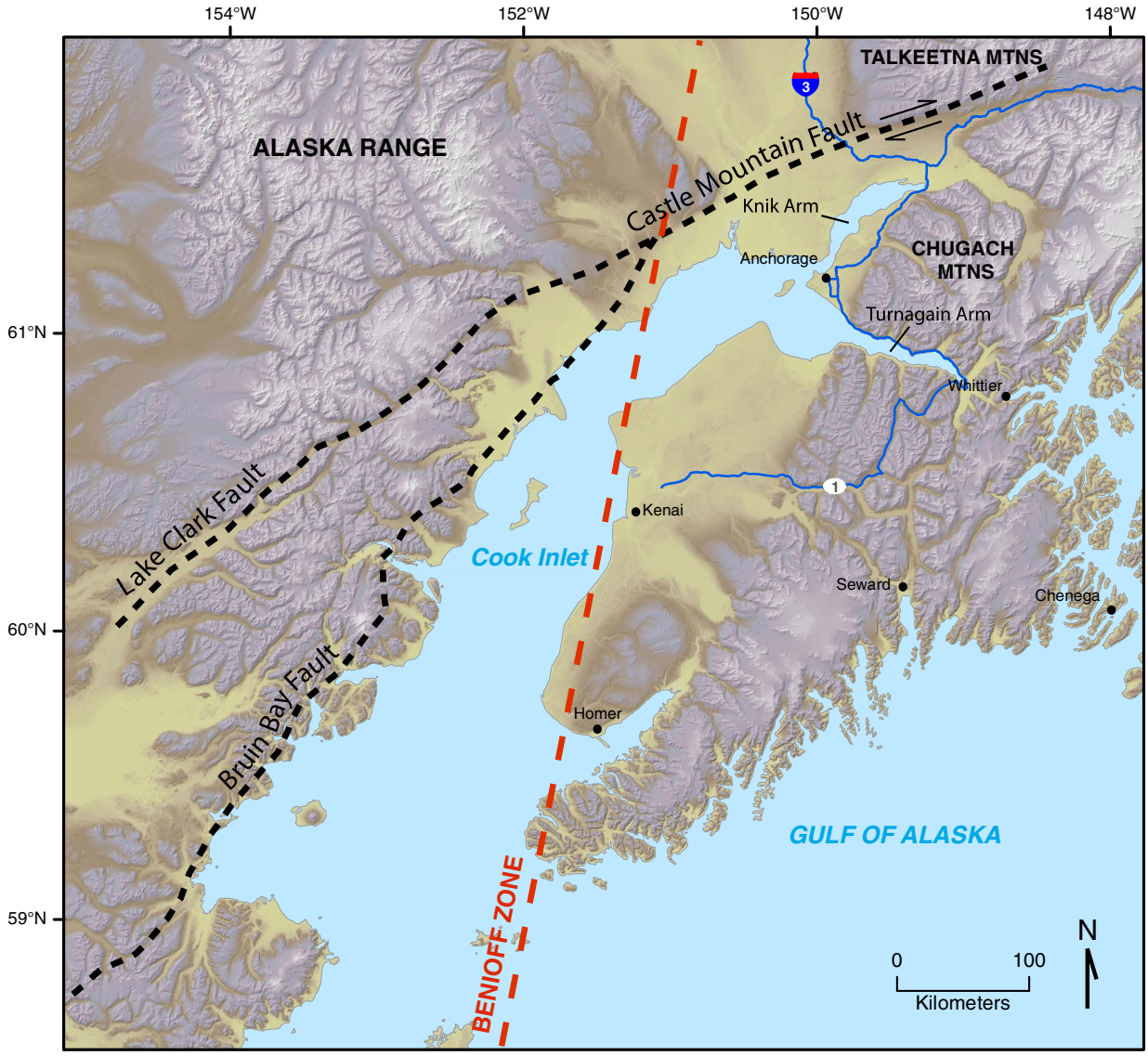

Fig. 2. Known faults in the vicinity of Anchorage, Alaska, shown by dashed lines; major highways are denoted, and dots indicate cities. Location of the Benioff zone according to Plafker et al. (1994). (Adapted from Lade et al. 1988.)

Earthquake Data

On November 30, 2018, at 17:29:28 Coordinated Universal Time (UTC) (8:29:29 local time), a M_W 7.1 earthquake hit 12 km north of Anchorage, Alaska (Mosalam et al. 2018). The earthquake's hypocenter was located at 61.323° N, 149.923° W at a depth of 47 km (USGS 2018). The main shock occurred in the Alaska-Aleutian subduction zone and was caused by east–west tension along a roughly north–south-trending normal (tensional) fault within the subducting Pacific slab (Stein et al. 2018). This event was followed by hundreds of aftershocks with various magnitudes. More than 80 aftershocks were recorded with a magnitude greater than 3.0 throughout the first day. The largest aftershock with M_W 5.7 occurred 6 min after the main shock about 4.8 km north of Anchorage.

In addition to the main shock (M_W 7.1), six aftershocks with moment magnitude between 4.2 and 5.7 were identified for this study based on their proximity to the site and the recordings' intensity. The distant aftershocks or aftershocks with smaller magnitudes were discarded. The events selected are listed in Table 1 along with distance and epicenter values. The event epicenters are depicted on a regional map in Fig. 5. These events were 21–44 km deep, and about half of them are considered as far field because they were recorded at epicenter distances larger than 20 km. All earthquake data have a sampling rate of 200 samples per second (sps). The M_W 5.7 aftershock is the closest event with a peak ground acceleration (PGA) of 0.042 g, recorded at an epicenter distance of 5.3 km. The largest PGA of 0.25 g (Fig. 6) was recorded during the main shock at an epicenter distance of 14.3 km. Fig. 6 shows the north–south direction motions from glacial till amplify as they propagate within the BCF, and deamplify within the transition region to glacial outwash due to impedance contrast.

Methodology

The deconvolution of the response of the soil column obtained at a depth $z1$ with that at depth $z2$ is defined in the frequency domain as

$$S(w,z) = \frac{u(z1,w)}{u(z2,w)} \quad (1)$$

Downloaded from ascelibrary.org by Harbin Institute of Technology on 10/24/20. Copyright ASCE. For personal use only; all rights reserved.

Downloaded from ascelibrary.org by Harbin Institute of Technology on 10/24/20. Copyright ASCE. For personal use only; all rights reserved.

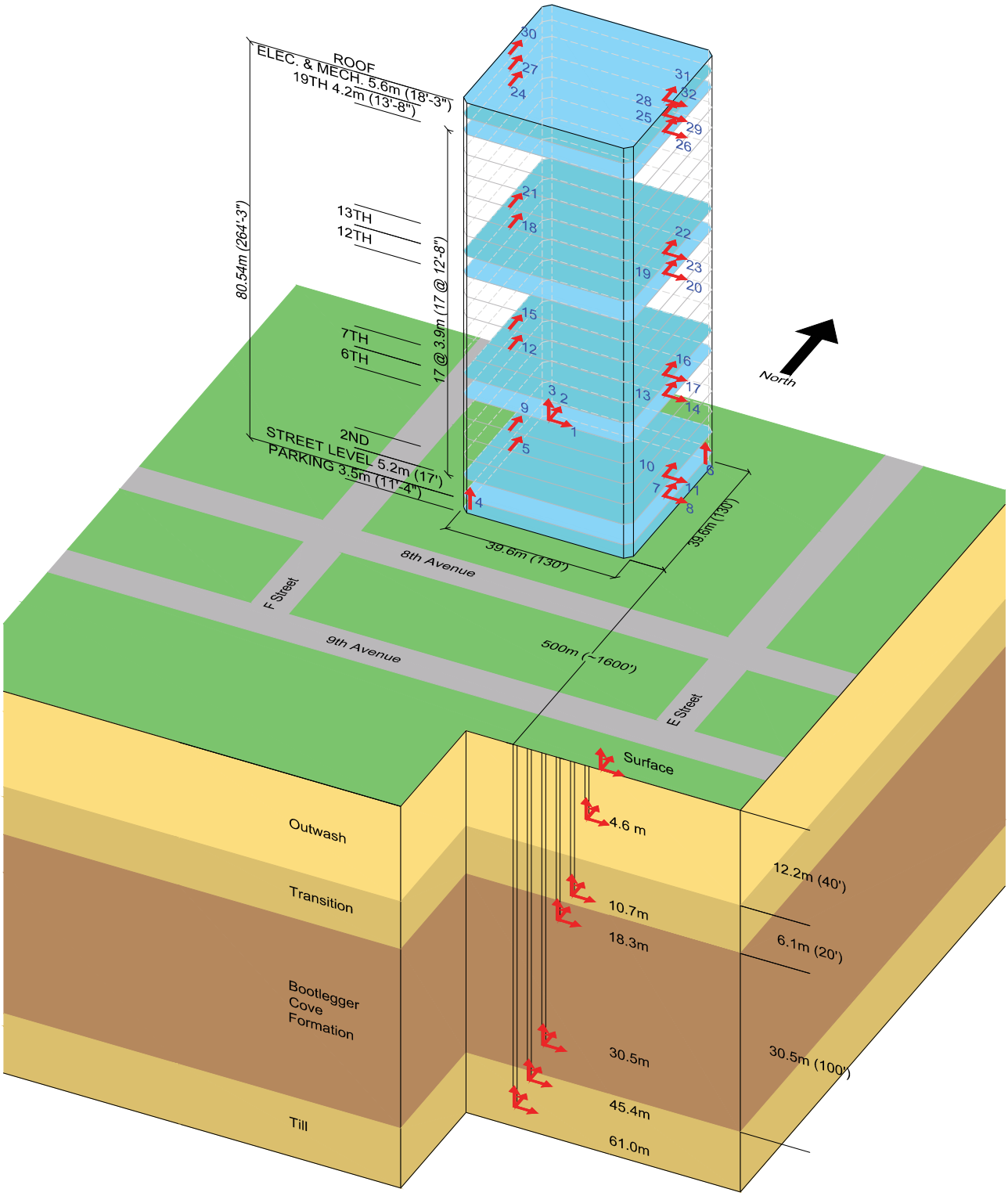

Fig. 3. Instrumentation layout of Delaney Park borehole array and soil layers; arrows indicate sensor orientation. Also shown is the instrumentation layout of the Atwood Building.

where $u(z1, w)$ and $u(z2, w)$ = Fourier spectra of the motions recorded at depths $z1$ and $z2$, respectively. This equation may become ill conditioned when the denominator approaches zero due to data corrupted by noise. In order to eliminate the instability, a regularized format following the Tikhonov deconvolution $S_\varepsilon(\omega)$ is used (Tikhonov and Arsenin 1977; Mehta et al. 2007a, b; Parolai et al. 2009; Petrovic and Parolai 2016)

$$S_\varepsilon(\omega) = W_\varepsilon \frac{u(z1, w)}{u(z2, w)} \tag{2}$$

where W_ε is the regularization function defined as

$$W_\varepsilon(\omega) = \frac{|u(z2, w)|^2}{|u(z2, w)|^2 + \varepsilon} \tag{3}$$

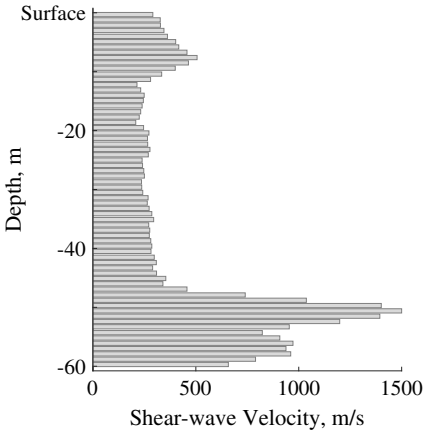

Fig. 4. Shear-wave velocity profile of the DPK array based on downhole velocity profiling measurements by Thornley et al. (2019). Shear-wave velocity is lower between −20 and −48 m at the Bootlegger Cove Formation than the shallower glacial outwash (between 0 and −12.2 m). See Fig. 3 for the geological profile.

in which ε = regularization parameter—a constant added to the denominator to avoid the numerical instability of Eq. (1). The value of ε was assumed to be 1% of the average spectral power.

Results

We applied deconvolution interferometry to the data from the seven earthquakes listed in Table 1. The soil responses from six boreholes were deconvolved by the soil response measured at the surface. The deconvolution results were based on the north–south and east–west component of the horizontal motions. Both horizontal components of records produced similar results. Fig. 7 shows the deconvolved waveforms after performing deconvolution of subsurface waves with the waves at the surface. Full lengths of the waveforms in Fig. 6, low-cut filtered by a second-order acausal Butterworth filter with corner frequency of 0.1 Hz, were utilized. This is consistent with the results of Mehta et al. (2007a, b) and Parolai et al. (2009), who showed the independence of the deconvolution results of the signal window used. This way, it is anticipated that the deconvolved waves are primarily related to the S-phase.

The deconvolved wave at the surface is a bandpass-filtered Dirac delta function (virtual source) because any waveform deconvolved with itself, with white noise added, yields a Dirac delta function (pulse) at $t = 0$. The deconvolved waveforms at Boreholes 2 through 6 demonstrate a wave state of the borehole array. This wave state is the response of different soil layers to the delta function at the surface. For early times (i.e., $t < 0$), the pulse travels upward in the soil column with a velocity equal to shear-wave velocity of soil layers. At $t = 0$, the wave field is nonzero only at the surface. For later times (i.e., $t > 0$), however, the pulse travels downward in the soil column, and the waveforms are governed by site resonance that decays exponentially with time due to attenuation (intrinsic damping).

The deconvolved waves in Fig. 7 do not show notable intrinsic damping, but some pulse broadening is noticeable. This is consistent with the soil-damping ratio computed as described in the section "Soil-Damping Ratio."

Shear-Wave Velocity

The shear-wave velocity of the upward and downward traveling waves ($V_{S,n}$) for the nth layer between two boreholes was derived based on the time lag τ between deconvolved waveforms and the distance h between observation points following the ray theory, which ignores wave scattering, $V_{S,n} = h/\tau$. The wave travel time associated with the first borehole at −4.6 m was discarded because of the overlapping upward and downward waves at this level. In Fig. 8(a), the arrival time and travel distance of the upward and downward traveling waves are identified to estimate the shear-wave velocity profiles based on the M_W 7.1, M_W 4.8, and M_W 5.7 earthquake waveforms. These events have the largest horizontal PGA recorded at the surface level (Table 1).

Interpolating the deconvolved waveforms to a higher sampling rate before peak picking reduces the picking error. For this reason, we interpolated the deconvolved waveforms (sampled originally at 200 sps) to 1,000 sps. The interpolation process applies an antialiasing (low-pass) finite impulse response (FIR) filter to time series with a Kaiser window (Oppenheim et al. 1999). The linear-phase FIR filter minimizes the weighted, integrated squared error between an ideal piecewise linear function and the magnitude response of the filter over a set of desired frequency bands (Parks and Burrus 1987).

In Fig. 8(a), the negative values are due to the upward traveling waves and the positive values are associated with the downward traveling waves. By using the time difference (tp) in the unit of seconds between the peaks of deconvolved waveforms between two consecutive layers, shear-wave velocity profiles were estimated. Fig. 8(b) depicts such profiles from upward (continuous thick vertical lines) and downward (dashed thick vertical lines) traveling waves with logged data (horizontal bars). In this figure, thin vertical lines denote propagated measurement error in shear-wave

Table 1. Origin times, magnitudes, and epicenter locations of main shock and aftershocks recorded by the Delaney Park borehole array in Anchorage, Alaska, in 2018 Anchorage earthquake sequence

			Epicenter coordinates				Peak acceleration (cm/s^2)	
Event	Origin time (UTC)	Moment magnitude	Latitude (° N)	Longitude (° W)	Depth (km)	Epicenter distance (km)	North–south	East–west
1	November 30, 2018, 17:29:29	7.1	61.340	−149.937	40	14.3	245.6	247.3
2	November 30, 2018, 17:33:52	4.8	61.363	−149.880	44	16.7	36.0	48.5
3	November 30, 2018, 17:35:37	5.7	61.259	−149.921	39	5.3	36.0	48.5
4	November 30, 2018, 17:43:00	4.5	61.516	−149.908	41	33.7	6.3	5.1
5	November 30, 2018, 19:26:30	4.9	61.394	−149.972	38	20.5	11.4	15.6
6	November 30, 2018, 20:26:56	5.1	61.392	−150.064	31	21.9	11.2	22.8
7	November 30, 2018, 23:07:47	4.2	61.472	−150.026	21	29.6	2.6	4.1

Note: Earthquakes are numbered sequentially according to their origin times. Peak acceleration is the observed absolute maximum amplitude of the waveforms from the north–south accelerometers at the surface level.

Downloaded from ascelibrary.org by Harbin Institute of Technology on 10/24/20. Copyright ASCE. For personal use only; all rights reserved.

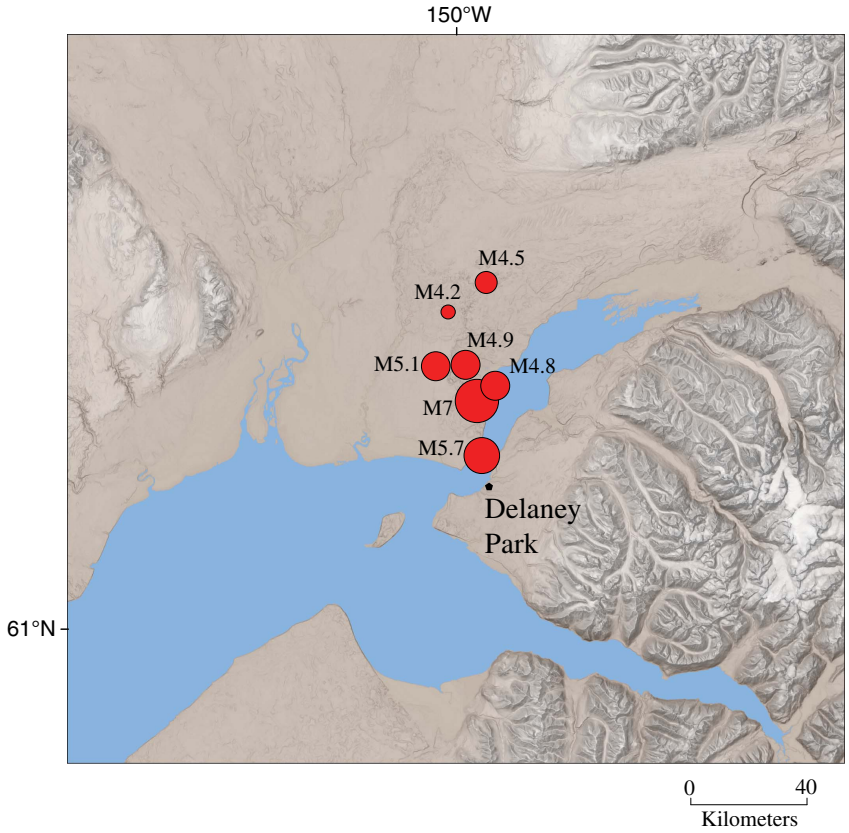

Fig. 5. Location of DPK array (61.21349° N and 149.98328° W) and epicenters of the main shock and six aftershocks with circles (summarized in Table 1). (Map data from Esri, DeLorme, HERE, MapmyIndia.)

velocity (dV_S) due to sampling rate ($dt = 0.005$ s, corresponding to 200 sps) uncertainty. By assuming independent random errors and exact height measurements between layers, dV_S is computed as

$$dV_S = V_S \frac{dt}{tp} \tag{4}$$

The term *layer* used here does not necessarily refer to soil layers with distinct physical parameters but the soil medium between tips of two boreholes where the accelerometers are located, which are shown by dashed horizontal lines in Figs. 8(a and b).

The shear-wave velocities of the five layers estimated from upward and downward traveling waves from different earthquakes are close to each other between different events; these values are summarized in Table 2. The difference of velocity for upward and downward traveling waves is due to attenuation (and possible anelasticity). The damping itself affects the pulse propagation being dispersed. For lightly damped systems, this effect is small.

Also listed in Table 2 are dV_S values following the $\pm$ sign. The dV_S is largest for the first event at the deepest borehole, which is equal to ± 216 m/s. At other borehole levels, dV_S is much smaller. The last row of this table provides mean shear-wave velocity values of each layer and uncertainty in the mean (σ) considering seven earthquakes. The value of σ is computed as

$$\sigma = \frac{1}{7}\sqrt{\sum_{eq=1}^{7} (dV_{S,eq})^2} \tag{5}$$

where eq = earthquake ID. The largest value of σ from different events is 187 m/s at Layer 5 (24% of mean V_S value).

In order to determine a single average shear-wave velocity for the upper 61 m of the soil, a line was fitted to all picked data points [Fig. 8(a)] by least squares [Fig. 8(c)]. This process was repeated by randomly adding time uncertainty ($dt = 0.005$ s) to time pairs via Monte Carlo simulation. A total of 1,000 simulations were performed. The time uncertainty was assumed to have a uniform distribution between -0.005 and 0.005 s. This way, measurement errors were propagated to the average shear-wave velocities, which are listed in Table 3. The average shear-wave velocities from the aftershocks are similar, with a standard deviation of 2.0 m/s. Although not reported here, the average shear-wave velocities of the aftershocks are also analogous to those obtained from 10 historical events between 2006 and 2013 (magnitudes vary from 4.5 to 5.4, and peak ground accelerations vary from 1.07 to 30.53 cm/s^2) (Wen and Kalkan 2020). These comparisons collectively point to recoverable nonlinear response associated with the 2018 main shock.

Fig. 9 compares estimated μ (thick vertical lines) and $\mu \pm \sigma$ (thin vertical lines) shear-wave velocity profiles from upward (continuous vertical lines) and downward (dashed vertical lines) traveling waves using seven earthquakes with logged data (horizontal bars). The dashed horizontal lines indicate depths of borehole sensors. Also shown in this figure are the errors in shear-wave velocity estimates as compared to the average of logged data between boreholes. The deconvolution interferometry predicts the shear-wave velocities within 27% of the logging data for upward-traveling waves and within 31% of logging data for downward-traveling waves. As a reference, the mean value of shear-wave velocity from seven earthquakes computed using the least-square fit (Table 3) is displayed in this figure as vertical dotted lines. The mean value is in

Downloaded from ascelibrary.org by Harbin Institute of Technology on 10/24/20. Copyright ASCE. For personal use only; all rights reserved.

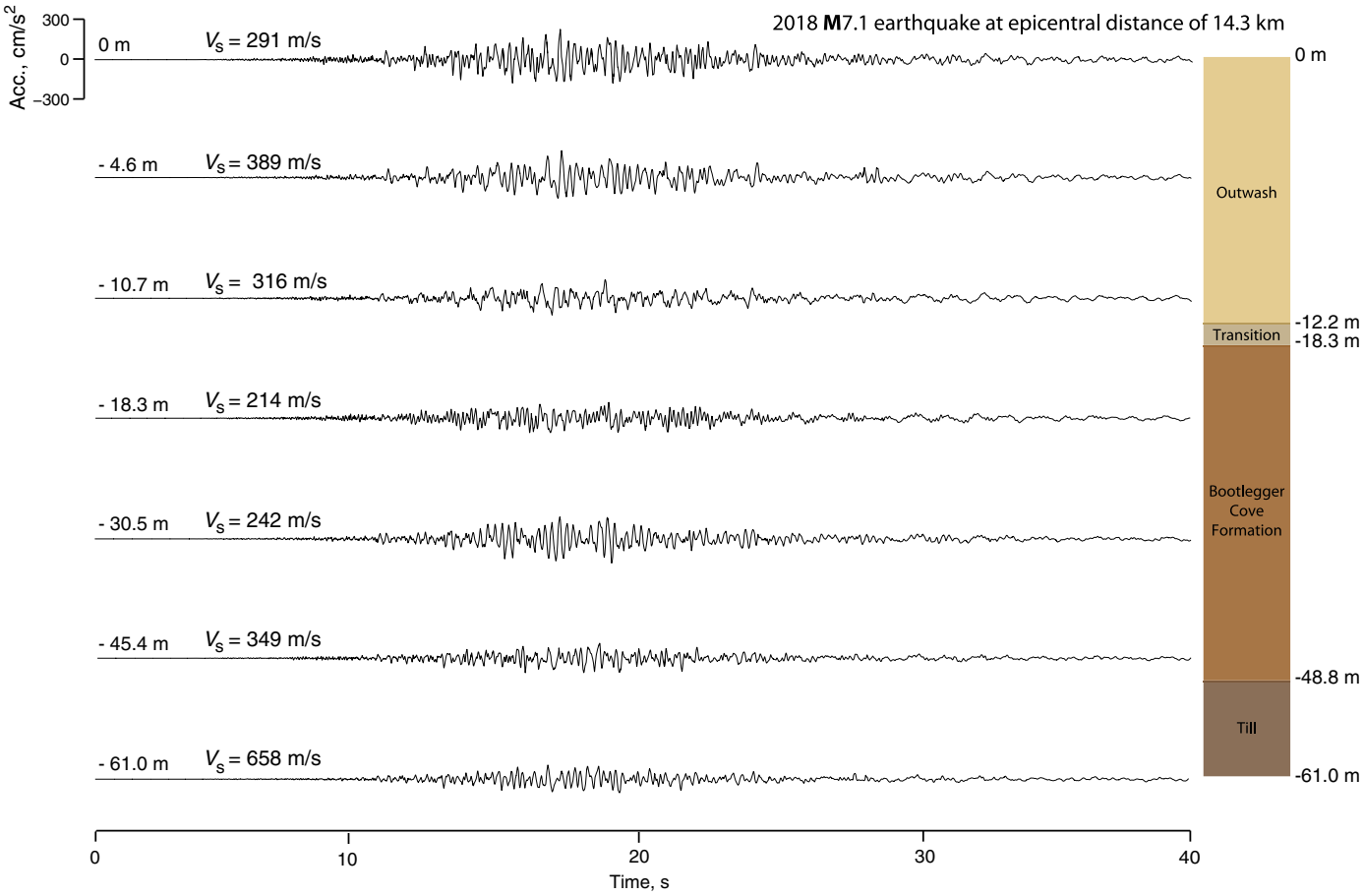

Fig. 6. Horizontal acceleration waveforms in north–south direction from the 2018 M_W 7.1 earthquake at epicenter distance of 14.3 km; recorded peak ground acceleration at the surface is 245.6 cm/s^2; soil layers and their shear-wave velocity (V_S) values from in situ measurements of Thornley et al. (2019) are depicted. Only the first 40 s of the waveforms are shown to distinguish P- and S-phases.

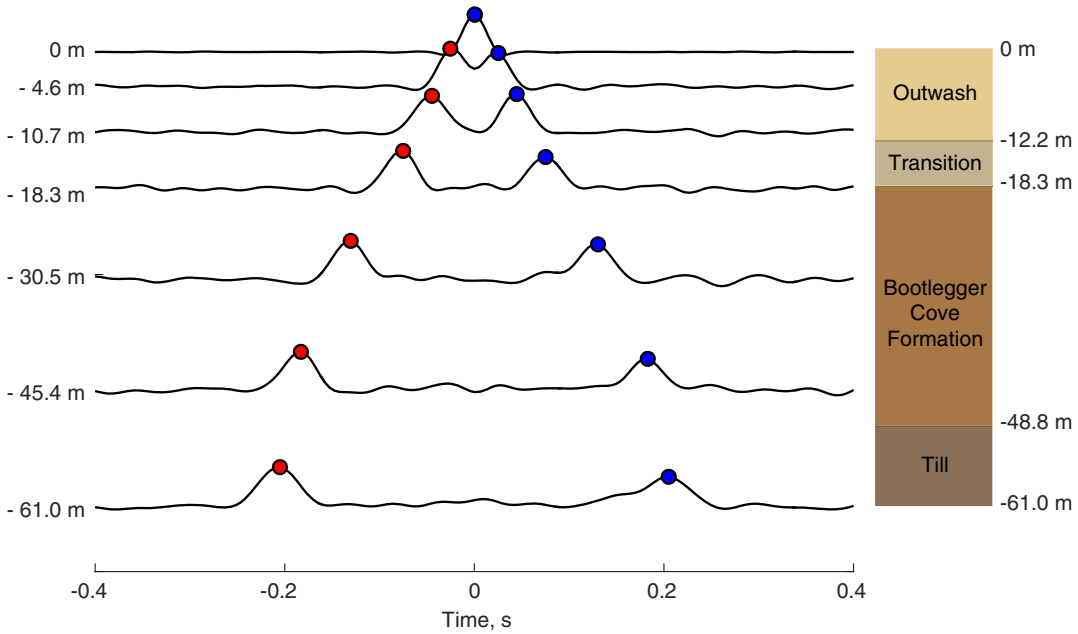

Fig. 7. Waveforms in Fig. 6 at different depths after deconvolution with the waveform recorded at the surface. The deconvolved waveforms by the surface response are acausal and show the upward and downward traveling waves. At the second depth (close to the surface) these waves are not distinguishable due to overlapping. Soil layers are depicted.

J. Geotech. Geoenviron. Eng., 2021, 147(1): 04020150

Downloaded from ascelibrary.org by Harbin Institute of Technology on 10/24/20. Copyright ASCE. For personal use only; all rights reserved.

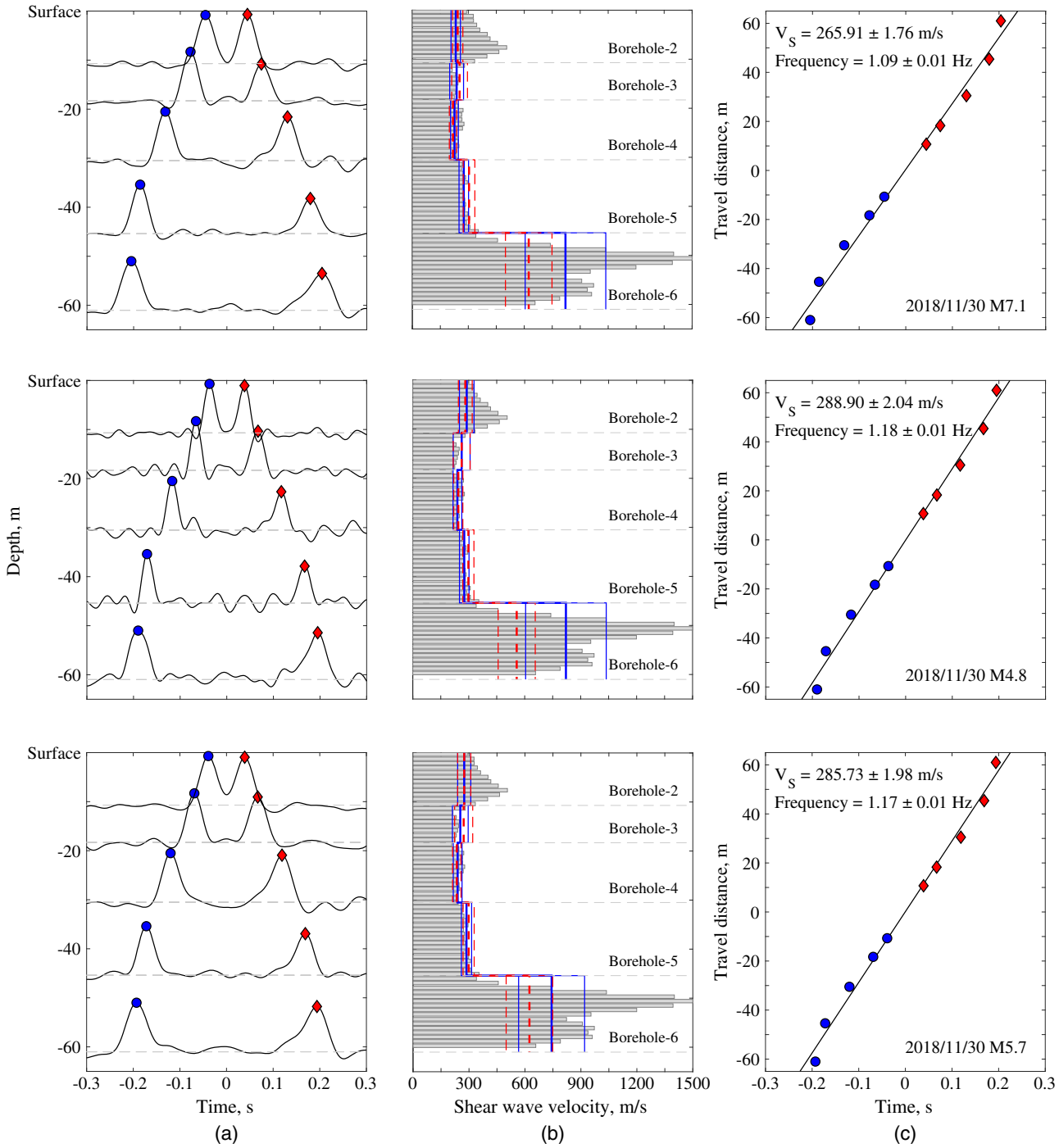

Fig. 8. (a) Arrival times of upward and downward traveling waves at five borehole levels (dashed line) estimated from the peaks of the deconvolved waves (circles are for upward and diamonds are for downward traveling waves); (b) comparisons of estimated shear-wave velocity profiles from upward (continuous thick vertical lines) and downward (dashed thick vertical lines) traveling waves with logged data (horizontal bars); thin vertical lines denote propagated measurement error due to sampling rate uncertainty; (c) an average shear-wave velocity (V_S) for the upper 61 m of soil column derived from the estimated travel times and the distances following a least-square fit. Average site frequency is computed from $V_S/4H$ (H = depth of soil column); ± denotes measurement error due to sampling rate uncertainty determined by Monte Carlo simulations. Results are based on the 2018 M_W 7.1, M_W 4.8, and M_W 5.7 earthquake waveforms.

general close to the logged data. The average error is about 15%, which is moderate.

Predominant Frequencies

For a homogenous isotropic shear column with a one-dimensional wave-propagation model, the predominant site frequency (f) can be derived from V_S as $f = V_S/4H$, where H is the total height. The arithmetic mean value of V_S from seven earthquakes (Table 3) yields $f = 1.17 \pm 0.04$ Hz. For comparison, the predominant site frequencies were also identified by computing the surface-to-borehole SSR.

The SSR was computed as the ratio of the Fourier spectra of the surface recording to those of the deepest borehole because it

J. Geotech. Geoenviron. Eng., 2021, 147(1): 04020150

Downloaded from ascelibrary.org by Harbin Institute of Technology on 10/24/20. Copyright ASCE. For personal use only; all rights reserved.

Table 2. Shear-wave velocity of soil layers identified based on upward and downward traveling waves

	Layer 1 (0–10.7 m)		Layer 2 (10.7–18.3 m)		Layer 3 (18.3–30.5 m)		Layer 4 (30.5–45.4 m)		Layer 5 (45.4–61 m)	
Event	Up	Down	Up	Down	Up	Down	Up	Down	Up	Down
1	233 ± 25	243 ± 28	238 ± 37	253 ± 42	226 ± 21	218 ± 19	276 ± 26	304 ± 31	821 ± 216	624 ± 125
2	289 ± 39	282 ± 37	262 ± 45	262 ± 45	239 ± 23	244 ± 24	276 ± 26	298 ± 30	821 ± 216	557 ± 99
3	274 ± 35	274 ± 35	253 ± 42	271 ± 48	239 ± 23	235 ± 23	287 ± 28	298 ± 30	743 ± 177	624 ± 125
4	297 ± 41	289 ± 39	262 ± 45	262 ± 45	239 ± 23	239 ± 23	281 ± 27	298 ± 30	743 ± 177	678 ± 147
5	297 ± 41	289 ± 39	253 ± 42	271 ± 48	239 ± 23	230 ± 22	287 ± 28	298 ± 30	709 ± 161	650 ± 135
6	289 ± 39	282 ± 37	253 ± 42	281 ± 52	244 ± 24	230 ± 22	292 ± 29	304 ± 31	709 ± 161	678 ± 147
7	289 ± 39	297 ± 41	281 ± 52	271 ± 48	235 ± 23	235 ± 23	287 ± 28	292 ± 29	780 ± 195	709 ± 161
Mean	281 ± 38	279 ± 37	257 ± 44	267 ± 47	237 ± 23	233 ± 22	283 ± 27	298 ± 30	761 ± 187	646 ± 136

Note: Values given in m/s; ± indicates measurement error due to sampling rate uncertainty.

Table 3. Average shear-wave velocity of soil column identified based on upward- and downward-traveling waves

Event	Average shear-wave velocity of soil column (m/s)		Uncertainty (m/s)
1	265.9	±	1.75
2	288.8	±	2.0
3	285.8	±	1.9
4	291.4	±	2.1
5	289.9	±	2.1
6	291.2	±	2.1
7	293.3	±	2.0
Mean	286.3	±	1.99
Standard deviation	9.23	±	0.13

Note: The ± indicates measurement error due to sampling rate uncertainty determined by Monte Carlo simulations.

is embedded in the engineering bedrock (glacial till). The waveforms were bandpass filtered by a second-order Butterworth filter with cutoff frequencies of 0.2 and 20 Hz to filter out high and low frequencies. The ratio of the Fourier amplitude spectrum (FAS) of two noisy records is very sensitive to noise and would have unrealistically high amplitudes if no smoothing was performed on the FAS prior to taking the ratio. Thus, we applied a 50-point moving average filter with a length of 2.5 s in smoothing the FAS.

Fig. 10 presents the results from these methods for the north–south component of the records. For the SSR, the surface and deepest borehole recordings in the north–south direction were used. The shaded zones indicate the range of the first three fundamental frequencies, which are 1.2–1.4 Hz for the first mode, 3.7–4.1 Hz for the second mode, and 6.5–7.0 Hz for the third mode. The average ratios of the second and third frequencies to the predominant frequency are 3 and 5.2, respectively, while the corresponding analytical ratios are 3 and 5 for the uniform soil column.

The analytical SSR of the layered soil (assuming an equivalent linear approach) was also computed by using SHAKE2000. The recording of the deepest borehole was utilized as input, and the V_S profile from the seismic interferometry was used to quantify the shear modulus. The analytical SSR results as the ratio of the Fourier spectra of the simulated surface recordings to those of recorded borehole recordings considering all events are presented in Fig. 11. The spectra from the analytical SSR is much smoother as expected, and the peaks are close to locations shown in Figs. 10 and 11. To compare the analytical results with the measured ones, Table 4 lists the vibration frequencies identified by a simple wave-propagation method $[V_S/(4H)]$, and the measured and analytical SSR for Modes 1, 2, and 3 using recorded horizontal motions along the north–south direction. The predominant frequency derived from the simple wave-propagation method is a crude estimation that is less accurate than the estimation from the SSR. The difference between the analytical and measured SSR results are on average less than 10%. Although not shown here for brevity, the east–west direction recordings yield similar results.

As mentioned, the equivalent linear approach was used to compute the seismic response of layered soil. Besides the shear-wave velocity identified from interferometry, other dynamic parameters (e.g., density and modulus) were needed in the equivalent linear approach. The differences of assumed and actual values of these parameters would be one of the reasons for differences in amplitudes of spectral peaks. Also, the equivalent linear approach tends to restrain the seismic response of layered soil in the high-frequency band, which may be another reason for the differences.

Borehole Amplification

Borehole amplification refers to the increase in amplitude of seismic waves as they propagate through soft soil layers; this increase is the result of impedance contrast (impedance = density of soil × V_S) between different layers (Safak 2001). In this study, the borehole amplification is calculated by SSR, c-SSR, and surface-to-borehole RSR.

The borehole recording is influenced by the downward waves reflected by the soil layers above, and the destructive interference among these waves may cause unexpected peaks in the spectral ratios (Shearer and Orcutt 1987). When shallow borehole data are used as a reference for estimating amplification at the surface, the potential maximum in the borehole spectrum would produce peaks in the spectral ratios that could be miscalculated as site-response peaks. The coherence estimates $C_{xy}(f)$ between the surface- and borehole-recorded signals may be used to identify the destructive interference effects. Such effects manifest as artificial peaks in the surface-to-borehole transfer function. These artificial peaks correspond to the sinks in the coherence estimate.

In order to eliminate the effects of the destructive interference on site amplification, we computed the c-SSR, which is the product of the spectral ratio and the coherence function (Safak 1997) to estimate the site amplification. The coherence $C_{xy}(f)$ of the surface recording and borehole recording is computed as

$$C_{xy}(f) = \frac{|P_{xy}(f)|^2}{P_{xx}(f)P_{yy}(f)} \tag{6}$$

where P_{xy} = cross-power spectral density of the response measured at the surface and borehole; and P_{xx} and P_{yy} = power spectral density of the response measured at the surface and borehole, respectively. The values of $C_{xy}(f)$ tending to 1 indicate that the corresponding frequency components are well correlated, whereas

Downloaded from ascelibrary.org by Harbin Institute of Technology on 10/24/20. Copyright ASCE. For personal use only; all rights reserved.

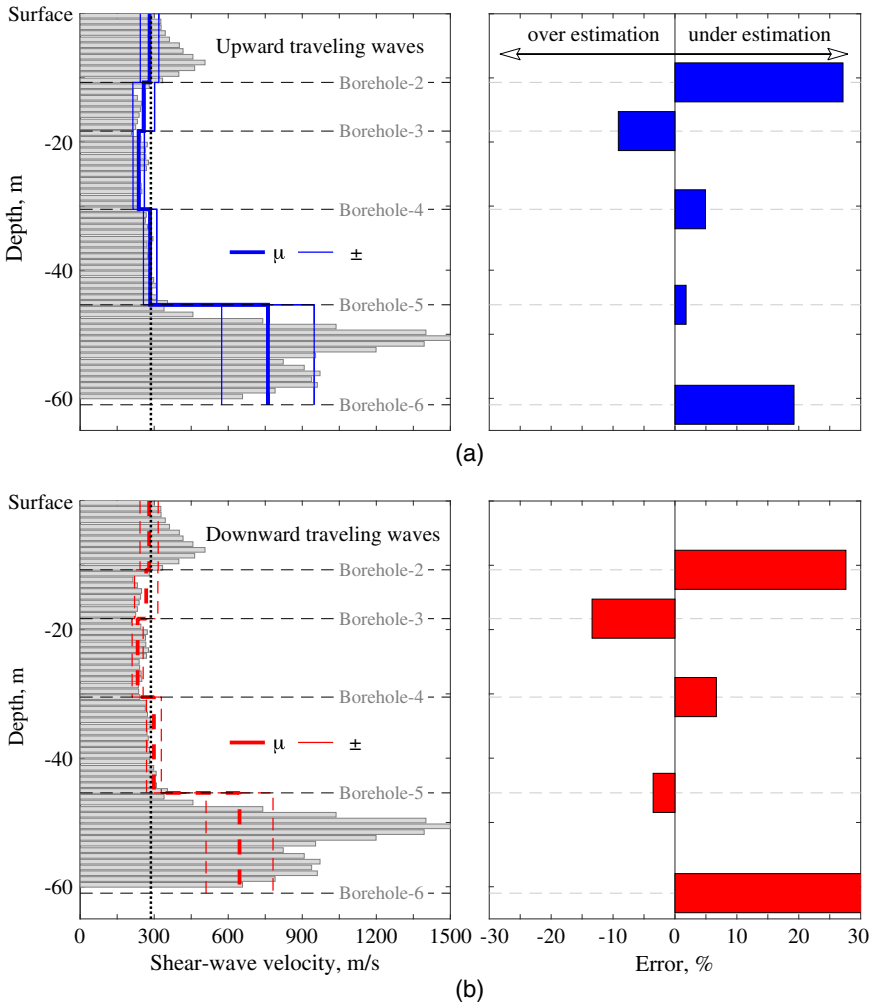

Fig. 9. Comparisons of estimated mean (μ) (thick vertical lines) and $\mu \pm$ one standard deviation (σ) (thin vertical lines) shear-wave velocity profiles from (a) upward (continuous vertical lines); and (b) downward (dashed vertical lines) traveling waves using seven earthquakes with logged data (horizontal bars). The dashed horizontal lines indicate depths of borehole sensors. The vertical dotted line denotes the average shear-wave velocity from seven earthquakes using the least-square fit (Table 3). The errors in shear-wave velocity estimates are compared to the average of logged data between boreholes. The deconvolution interferometry predicts the shear-wave velocities within 27% of the logging data for upward-traveling waves and within 31% of logging data for downward-traveling waves.

values tending to 0 indicate that the corresponding frequency components are uncorrelated. Frequency ranges in the transfer function that are dominated by noise (typically high frequencies) demonstrate low coherence. At frequencies where sinks are observed in the coherence estimate, the resulting cross-spectral values of the transfer function are expected to deviate from the traditional spectral ratio, indicating the occurrence of destructive interference phenomena. Such phenomena (incoherence) can be due to noise or to natural physical processes such as wave passage, scattering, and extended source effects (Zerva 2009).

Finally, the RSR, defined as the ratio of 5% damped pseudo-spectral acceleration response spectrum on the surface to those on the deepest borehole, was used (Kitagawa et al. 1992). Pseudo-spectral acceleration response spectra and their ratios are much smoother functions of frequency than the standard spectral ratios because the damped single-degree-of-freedom system acts as a narrow-band filter.

For each of these methods, borehole amplifications at different frequencies were computed and averaged across the ensemble of recordings considering all events. Fig. 12(a) plots the mean estimates. The DPK array site has a shallow soft layer in the near surface with relatively constant shear-wave velocity (295 m/s; NEHRP Site Category D) due to the presence of BCF overlying a relatively homogeneous stiff formation with strong impedance contrast at 50-m depth (NEHRP Site Category B). In Fig. 12(a), the values on the horizontal axis are the reciprocals of the periods for the RSR. For each method, three obvious peaks can be seen at three frequency ranges: 1.1–1.6, 3.9–4.5, and 6.5–7 Hz, respectively. These peaks correspond to the soil column predominant frequencies for the first three modes.

The SSR method produced greater site amplification estimates than the c-SSR and RSR methods at low frequencies. The SSR method predicts the maximum site amplification as 5.3. This method is the least reliable because it is very sensitive to the noise level in the waveforms; thus, it is not appropriate for downhole recordings.

The maximum site amplification of 4.2 is predicted by the RSR method; this method is applicable at low frequencies (e.g., less than 4 Hz), but not for high frequencies. The c-SSR method resulted in maximum site amplification as large as 3.5 at low frequencies close to the first mode frequency. The average coherence estimates of the surface and the deepest borehole recordings are also presented in

Downloaded from ascelibrary.org by Harbin Institute of Technology on 10/24/20. Copyright ASCE. For personal use only; all rights reserved.

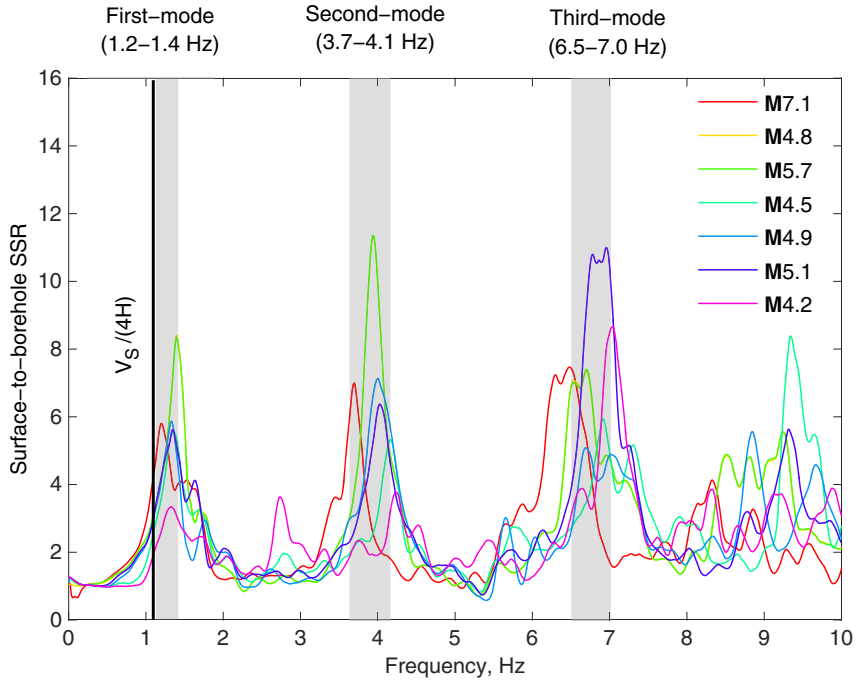

Fig. 10. First three fundamental mode frequencies of the soil column identified by surface-to-borehole SSR using the north–south recordings from seven earthquakes listed in Table 1. The shaded zones indicate the range of the first three fundamental frequencies. The vertical line indicates the reference site frequency from $f = V_S/4H$.

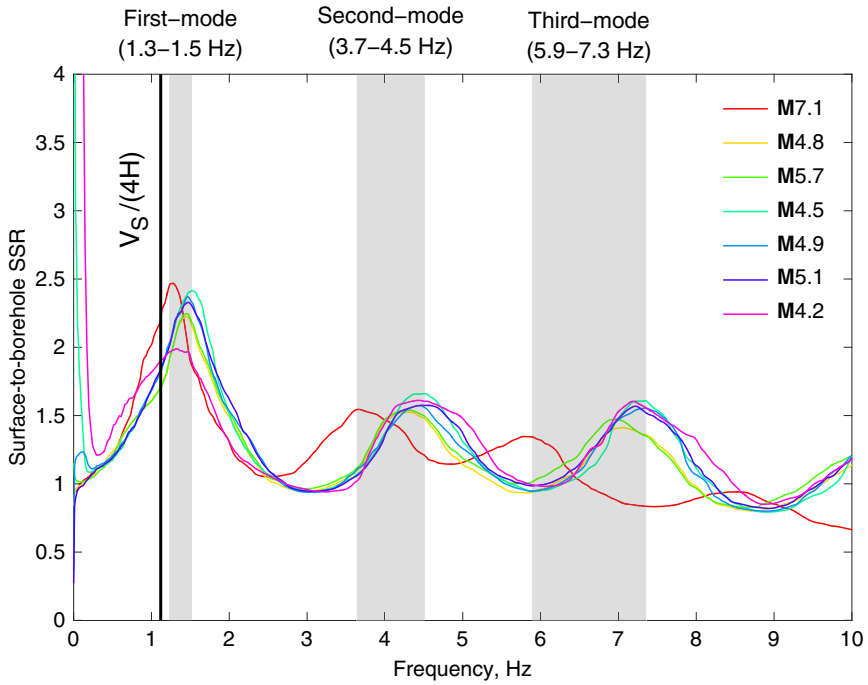

Fig. 11. First three fundamental mode frequencies of the soil column identified by analytical (assuming an equivalent linear approach) surface-to-borehole SSR using the deepest borehole recordings from the north–south direction from seven earthquakes listed in Table 1. The shaded zones indicate the range of the first three fundamental frequencies. The vertical line indicates the reference site frequency from $f = V_S/4H$.

Fig. 12(b). Based on the equivalent homogeneous medium approach, the first mode frequency at which destructive interference is expected to occur is estimated as 1.2 Hz, which is also indicated in Fig. 12 with the solid arrow. Clearly, the destructive interference phenomenon is not strictly materialized, which may be due to the variation of the shear-wave velocity among different soil layers as can be seen in Fig. 9. However, the dashed arrows in Fig. 12 indicate that peak site amplification predicted by the c-SSR method generally corresponds to the sinks of coherence (low-coherence) estimates. The low coherence corresponds to the maximum

J. Geotech. Geoenviron. Eng., 2021, 147(1): 04020150

Downloaded from ascelibrary.org by Harbin Institute of Technology on 10/24/20. Copyright ASCE. For personal use only; all rights reserved.

Table 4. Vibration frequencies identified by the simple wave-propagation method $[V_S/(4H)]$ and measured and analytical surface-to-borehole SSR for Modes 1, 2, and 3 using recorded horizontal motions along north–south direction

Method	Mode	Event 1	2	3	4	5	6	7
$V_S/(4H)$		1.09	1.15	1.17	1.19	1.18	1.19	1.20
Measured SSR	Mode 1	1.20	1.40	1.40	1.38	1.31	1.34	1.37
	Mode 2	3.69	3.94	3.94	4.09	4.01	4.04	4.09
	Mode 3	6.48	6.61	6.61	6.91	6.72	6.87	7.03
Analytical SSR	Mode 1	1.26	1.46	1.46	1.48	1.46	1.46	1.48
	Mode 2	3.66	4.33	4.33	4.38	4.44	4.33	4.48
	Mode 3	5.88	7.06	6.96	7.23	7.33	7.06	7.23

Note: Surface and deepest borehole (at −61 m) recordings were used in SSR computations. Values given in hertz; V_S = shear-wave velocity; and H = height of soil column.

amplifications where spectral ratios of the surface and deepest borehole recordings have the largest difference. This phenomenon means that the c-SSR method can predict site amplification at low frequencies more reliably by removing the potential destructive interference.

Soil-Damping Ratio

During wave propagation, the energy loss induced by soil damping can be represented by the following attenuation equation (Aki and Richards 2002):

$$A_s(f) = e^{-\pi \cdot f \cdot \tau / Q} \tag{7}$$

where $A_s(f)$ = reduction in the amplitude of a sinusoidal wave of frequency f when it travels a distance of travel time τ. The damping ratio ξ is defined by the quality factor Q ($\xi = 1/2Q$).

In order to evaluate the dynamic damping in structures, previous studies (Snieder and Safak 2006; Prieto et al. 2010; Newton and Snieder 2012; Nakata et al. 2013) used Eq. (7) in conjunction with deconvolved waves. We adapted the same approach for evaluating the soil dynamic damping. First, the recordings at different soil layers were deconvolved with the recordings at the deepest borehole, and then the deconvolved waves were bandpass filtered by a second-order Butterworth filter with cutoff frequencies of 0.5 and 2 Hz. These corner frequencies were selected to extract the fundamental mode, and filtered out high and low frequencies. The natural logarithm of the envelope of the bandpass-filtered waveforms corresponding to the M_W 7.1 event is shown in Fig. 13. In order to separate the curves at different borehole depths, the natural logarithm of the envelope is added with the number of 50 minus the depth of the borehole (the depth is 0 at the surface). According to Eq. (7), the slope of the curves in Fig. 13 depends on the attenuation of the waves; thus, the offset has no influence on the results. The slopes of the curves, which are similar at different layers, were computed by least-square fit between 0.5 and 5.5 s (shown by thick lines). The slope of the solid line is equal to $-\pi f/Q$. The mean slope at different layers (which is quite consistent at different depths) and the first mode frequencies were used to compute Q and ξ. Table 5 summarizes the resultant Q and ξ for all events. The results are stable between different events with a coefficient of variance (COV) of 0.09 for Q. The average soil dynamic damping for the DPK array was found to be 4.8%. The damping ratio corresponding to the main shock is higher than aftershocks due to the recoverable nonlinear response.

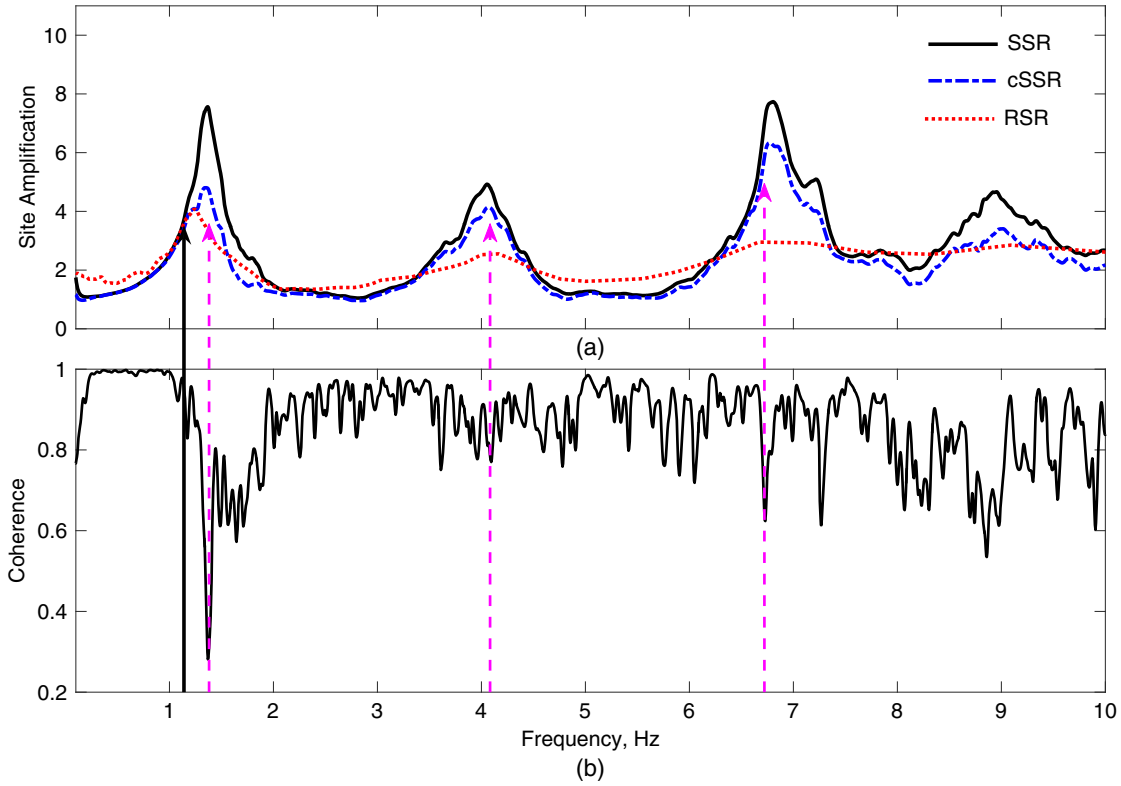

Fig. 12. (a) Average site amplification estimates of recordings from seven earthquakes calculated by four different methods (surface-to-borehole traditional (SSR), RSR, and (c-SSR); and (b) average magnitude-squared coherence estimates of the surface and the deepest borehole recordings. The solid arrow indicates the first mode frequency with high coherence; the dashed arrows denote the frequencies where the sinks of coherence estimate are observed due to destructive interference.

Downloaded from ascelibrary.org by Harbin Institute of Technology on 10/24/20. Copyright ASCE. For personal use only; all rights reserved.

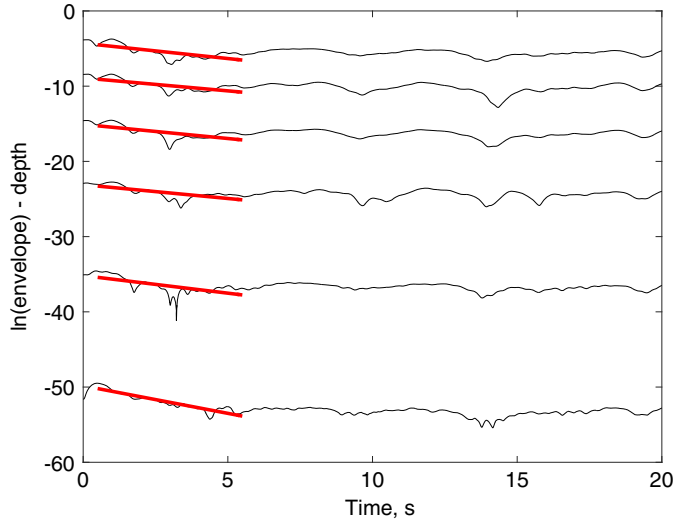

Fig. 13. Natural logarithm envelope of the bandpass-filtered waveforms (dashed lines), and their least-square fit between 0.5 and 5.5 s (solid lines). Data correspond to the M_W 7.1 earthquake as shown in Fig. 6. Deconvolved waves were bandpass filtered by a second-order acausal Butterworth filter with cutoff frequencies of 0.5 and 2 Hz.

Table 5. Mean slope of different layers, quality factor (Q), and intrinsic damping ratio (ξ) computed for different earthquakes

Event	Mean slope of different layers	Quality factor, Q	Damping ratio, ξ (%)
1	−0.45	9.04	5.53
2	−0.45	9.86	5.07
3	−0.44	9.91	5.04
4	−0.43	10.24	4.88
5	−0.40	10.51	4.76
6	−0.38	11.47	4.36
7	−0.38	11.82	4.23
Average		10.41	4.80
COV		0.09	0.09

Shear Modulus

In homogeneous and isotropic media, the velocity of a shear wave is controlled by the shear modulus G_n, which defines the magnitude of the shear stress that soil can sustain—an important parameter for geotechnical engineering applications. The shear modulus G_n for the nth soil layer is

$$G_n = \rho_n V_{S,n}^2 \tag{8}$$

where ρ_n = density of the nth layer. A wet density of 1.96 g/cm^3 was assigned to the BCF based on measurements of 10 soil samples (Lade et al. 1988). The site at which the undisturbed samples of the BCF were collected was found to be geologically typical of the 60 city blocks that form the core metropolitan area of Anchorage including the DPK array. Using Eq. (8) and averaged shear-wave velocity values of BCF (identified with the channels from 4.6 to 45.4 m), the shear modulus of the BCF at the DPK array was found to be between 121 and 144 MPa. The averaged shear-wave velocity values of BCF were obtained by computing the arithmetic mean of shear-wave values in Table 2 between Layers 1 and 4 considering upward and downward directions for each earthquake.

Conclusions

In this study, we investigated the properties of sediment layers, in particular the BCF at the DPK downhole array in downtown Anchorage, Alaska. BCF is a soft formation thought to be responsible for much of the ground failure during the 1964 M_W 9.2 Great Alaska earthquake (Thornley et al. 2019). The waveforms recorded from seven earthquakes of the 2018 M_W 7.1 Anchorage earthquake sequence (main shock and six aftershocks) were analyzed using deconvolution interferometry. The waveforms at various depths were deconvolved by the waveforms recorded at the surface in order to identify the shear-wave velocity profile, predominant frequencies, soil dynamic damping, and shear modulus. To quantify the site amplification, surface-to-borehole traditional SSR, RSR and c-SSR were calculated. The site characteristic information obtained here can be used for soil–structure interaction analysis of a nearby 20-story steel moment frame building (Atwood Building), which was also instrumented. The key findings of this study are as follows:

- The similarity of the deconvolved waveforms from seven earthquakes manifests that a one-dimensional shear-beam model is reasonable to represent the elastic soil response at the DPK array under low-intensity shaking.
- On average, deconvolution interferometry predicts shear-wave velocities within 27% of the logging data for upward-traveling waves and within 31% of logging data for downward-traveling waves. The uncertainties computed from different events are within 24% of mean shear-wave velocities. This suggests that deconvolution interferometry is an effective way to quantify the shear-wave velocity profile for geotechnical arrays lacking in situ measurements, providing that the vertical distribution of sensors sufficiently captures the complexity of the geologic structure.
- For all earthquakes, the predominant frequency derived from the shear-wave velocity of the soil column is on average 1.17 Hz, which is 10% smaller than the 1.3 Hz estimated from the c-SSR.
- Despite high aleatoric variability in earthquake waveforms, which come from events varying in size, distance, and azimuth, the average shear-wave velocity of soil layers and the predominant frequency of the soil column during aftershocks are consistent; this indicates the recoverable nonlinear site response during the mainshock.
- Destructive interference phenomena were demonstrated to yield overestimation of site response by means of the surface-to-borehole transfer function in the low-frequency range.
- The RSR method was found to be applicable for computing borehole amplification at low frequencies (less than 4 Hz) only; its accuracy quickly diminishes at high frequencies.
- The c-SSR method can predict site amplification more reliably by removing the potential destructive interference; thus, it is theoretically more accurate than the other methods. c-SSR resulted in average site amplification as large as 3.5 at low frequencies (1.1–1.6 Hz) close to the first mode frequency of the soil column. Other studies have found on average that the largest site amplifications are on the lower velocity NEHRP Class D ($180 < V_{S30} < 360$ m/s) sites in Anchorage, with average amplifications around 3 at low frequencies (0.5–2.5 Hz).

Data Availability Statement

Some or all data, models, or code generated or used during the study are available from the corresponding author by request. The fault lines in Fig. 2 were obtained from http://www.dggs.alaska.gov/pubs/id/24956 (last accessed August 2019), which

Downloaded from ascelibrary.org by Harbin Institute of Technology on 10/24/20. Copyright ASCE. For personal use only; all rights reserved.

included fault information from Koehler et al. (2012, 2013). Instruments of the National Strong Motion Network of USGS collected recordings used in this study. These recordings are available at http://nees.ucsb.edu/data-portal (last accessed August 2019). The MATLAB version R2018b of the deconvolution function used in this study is available at https://www.mathworks.com/matlabcentral/fileexchange/60644-deconvolution-of-two-discrete-time-signals-in-frequency-domain?s_tid=prof_contriblnk.

Acknowledgments

We thank two anonymous reviewers for their valuable comments, which helped improve the technical quality of this paper. Special thanks are extended to John Thornley for providing us in situ shear-wave measurements, Utpal Dutta and Joey Yang for discussions on DPK array soil properties, Luke Blair for generating the regional maps, and Shahneam Reza and Timothy Cheng for preparing the borehole array illustration. We are also grateful to Nori Nakata for fruitful discussions on deconvolution and for sharing his computer codes, which we modified significantly for this study.

Notation

The following symbols are used in this paper:

C_{xy} = coherence;
eq = earthquake ID;
G_n = shear modulus of nth layer;
H = total height of soil column;
n = layer ID;
P_{xx} = power spectral density of waveform x;
P_{xy} = cross-power spectral density of waveforms x and y;
Q = quality factor;
$S_\varepsilon(\omega)$ = deconvolution function;
t = time instant;
tp = time difference in peaks of deconvolved waveforms between two layers;
V_S = shear-wave velocity;
V_{S30} = average shear-wave velocity of upper 30 m of crust;
W_ε = regularization function;
w = cyclic frequency;
z = height;
ε = regularization parameter;
ξ = damping ratio;
ρ_n = wet density of nth layer;
σ = uncertainty in the mean value; and
τ = wave travel time.

References

Aki, K. 1957. "Space and time spectra of stationary stochastic waves, with special reference to microtremors." *Bull. Earthquake Res. Inst.* 35 (3): 415–456.

Aki, K., and P. G. Richards. 2002. *Quantitative seismology*. Mill Valley, CA: Univ. Science Books.

Bakulin, A., and R. Calvert. 2006. "The virtual source method: Theory and case study." *Geophysics* 71 (4): S139–S150. https://doi.org/10.1190/1.2216190.

Boore, D. M. 2004. "Ground motion in Anchorage, Alaska, from the 2002 Denali fault earthquake: Site response and displacement pulses." *Bull. Seismol. Soc. Am.* 94 (6): S72–S84. https://doi.org/10.1785/0120040606.

Borcherdt, R. D. 1970. "Effects of local geology on ground motion near San Francisco Bay." *Bull. Seismol. Soc. Am.* 60 (1): 29–61.

Bruhn, R. L. 1978. *Holocene displacements measured by trenching the Castle Mountain Fault near Houston, Alaska*. Alaska Division of Geological and Geophysical Surveys Geologic Rep. 61A. Fairbanks, AK: Alaska Division of Geological & Geophysical Surveys.

Claerbout, J. F. 1968. "Synthesis of a layered medium from its acoustic transmission response." *Geophysics* 33 (2): 264–269. https://doi.org/10.1190/1.1439927.

Finno, R. J., and D. G. Zapata-Medina. 2014. "Effects of construction-induced stresses on dynamic soil parameters of bootlegger cove clays." *J. Geotech. Geoenviron. Eng.* 140 (4): 04013051. https://doi.org/10.1061/(ASCE)GT.1943-5606.0001072.

Fogelman, K., C. Stephens, J. C. Lahr, S. Helton, and M. Allen. 1978. *Catalog of earthquakes in Southern Alaska, October-December, 1977*. US Geological Survey Open-File Rep. 78-1097. Reston, VA: USGS.

Hartman, D. C., G. H. Pessel, and D. L. McGee. 1974. "Stratigraphy of the Kenai group, Cook Inlet." Accessed August 10, 2019. http://www.dggs.alaska.gov/pubs/id/149.

Kitagawa, Y., I. Okawa, and T. Kashima. 1992. "Observation and analyses of dense strong motions at sites with different geological conditions in Sendai." In Vol. 1 of *Proc., Int. Symp. on the Effects of Surface Geology on Seismic Motions*. Yokohama, Japan: Association of Earthquake Disaster Prevention.

Koehler, R. D., P. A. C. Burns, and J. R. Weakland. 2013. *Digitized faults of the Neotectonic map of Alaska (Plafker and others, 1994)*. Fairbanks, AK: Alaska Division of Geological & Geophysical Surveys.

Koehler, R. D., R. E. Farrell, P. A. C. Burns, and R. A. Combellick. 2012. *Quaternary faults and folds in Alaska: A digital database*. Yokohama, Japan: Association of Earthquake Disaster Prevention.

Lade, P. V., R. G. Updike, and D. A. Cole. 1988. *Cyclic triaxial tests of the Bootlegger Cove formation, Anchorage, Alaska*. Washington, DC: US Government Printing Office.

Lahr, J. C., R. A. Page, C. D. Stephens, and K. A. Fogleman. 1986. "Sutton, Alaska, earthquake of 1984: Evidence for activity on the Talkeetna segment of the Castle Mountain fault system." *Bull. Seismol. Soc. Am.* 76 (4): 967–983.

Li, J., G. A. Abers, Y. Kim, and D. Christensen. 2013. "Alaska megathrust 1: Seismicity 43 years after the great 1964 Alaska megathrust earthquake." *J. Geophys. Res. Solid Earth* 118 (9): 4861–4871.

Lobkis, O. I., and R. L. Weaver. 2001. "On the emergence of the Green's function in the correlations of a diffuse field." *J. Acoust. Soc. Am.* 110 (6): 3011–3017. https://doi.org/10.1121/1.1417528.

Mehta, K., R. Snieder, and V. Grazier. 2007a. "Downhole receiver function: A case study." *Bull. Seismol. Soc. Am.* 97 (5): 1396–1403. https://doi.org/10.1785/0120060256.

Mehta, K., R. Snieder, and V. Grazier. 2007b. "Extraction of near-surface properties for a lossy layered medium using the propagator matrix." *Geophys. J. Int.* 169 (1): 271–280. https://doi.org/10.1111/j.1365-246X.2006.03303.x.

Mosalam, K., et al. 2018. *Steer—EERI Alaska earthquake: Preliminary virtual assessment team (P-Vat) joint report*. Miami: DesignSafe-CI.

Nakata, N., and R. Snieder. 2012. "Estimating near-surface shear wave velocities in Japan by applying seismic interferometry to KiK-net data." *J. Geophys. Res.* 117 (1): B01308. https://doi.org/10.1029/2011JB008595.

Nakata, N., R. Snieder, S. Kuroda, S. Ito, T. Aizawa, and T. Kunimi. 2013. "Monitoring a building using deconvolution interferometry. I: Earthquake-data analysis." *Bull. Seismol. Soc. Am.* 103 (3): 1662–1678. https://doi.org/10.1785/0120120291.

Nath, S. K., D. Chatterjee, N. N. Biswas, M. Dravinski, D. A. Cole, A. Papageorgiou, J. A. Rodriguez, and C. J. Poran. 1997. "Correlation study of shear wave velocity in near surface geological formations in Anchorage, Alaska." *Earthquake Spectra* 13 (1): 55–75. https://doi.org/10.1193/1.1585932.

Newton, C., and R. Snieder. 2012. "Estimating intrinsic attenuation of a building using deconvolution interferometry and time reversal." *Bull. Seismol. Soc. Am.* 102 (5): 2200–2208. https://doi.org/10.1785/0120110322.

Downloaded from ascelibrary.org by Harbin Institute of Technology on 10/24/20. Copyright ASCE. For personal use only; all rights reserved.

Oppenheim, A. V., R. W. Schafer, and J. R. Buck. 1999. *Discrete-time signal processing*. Upper Saddle River, NJ: Prentice Hall.
Parks, T. W., and C. S. Burrus. 1987. *Digital filter design*. New York: Wiley.
Parolai, S., A. Ansal, A. Kurtulus, A. Strollo, R. Wang, and J. Zschau. 2009. "The Ataköy vertical array (Turkey): Insights into seismic wave propagation in the shallow-most crustal layers by waveform." *Geophys. J. Int.* 178 (3): 1649–1662. https://doi.org/10.1111/j.1365-246X.2009.04257.x.
Petrovic, B., and S. Parolai. 2016. "Joint deconvolution of building and downhole strong-motion recordings: Evidence for the seismic wavefield being radiated back into the shallow geological layers." *Bull. Seismol. Soc. Am.* 106 (4): 1720–1732. https://doi.org/10.1785/0120150326.
Plafker, G., L. M. Gilpin, and J. C. Lahr. 1994. "Neotectonic map of Alaska." In Vol. G-1 of *The geology of North America: The geology of Alaska*, edited by G. Plafker and H. C. Berg, 389–449. Boulder, CO: Geological Society of America.
Prieto, G. A., J. F. Lawrence, A. I. Chung, and M. D. Kohler. 2010. "Impulse response of civil structures from ambient noise analysis." *Bull. Seismol. Soc. Am.* 100 (5A): 2322–2328. https://doi.org/10.1785/0120090285.
Rahmani, M., and M. I. Todorovska. 2013. "1D system identification of buildings from earthquake response by seismic interferometry with waveform inversion of impulse responses—Method and application to Millikan Library." *Soil Dyn. Earthquake Eng.* 47 (Apr): 157–174. https://doi.org/10.1016/j.soildyn.2012.09.014.
Roux, P., and M. Fink. 2003. "Green's function estimation using secondary sources in a shallow wave environment." *J. Acoust. Soc. Am.* 113 (3): 1406–1416. https://doi.org/10.1121/1.1542645.
Safak, E. 1997. "Models and methods to characterize site amplification from a pair of records." *Earthquake Spectra* 13 (1): 97–129.
Safak, E. 2001. "Local site effects and dynamic soil behavior." *Soil Dyn. Earthquake Eng.* 21 (5): 453–458. https://doi.org/10.1016/S0267-7261(01)00021-5.
Schuster, G. T., J. Yu, J. Sheng, and J. Rickett. 2004. "Interferometric daylight seismic imaging." *Geophys. J. Int.* 157 (2): 838–852. https://doi.org/10.1111/j.1365-246X.2004.02251.x.
Shearer, P. M., and J. A. Orcutt. 1987. "Surface and near-surface effects on seismic waves: theory and borehole seismometer results." *Bull. Seismol. Soc. Am.* 77 (4): 1168–1196.
Smart, K. J., T. L. Pavlis, V. B. Sisson, S. M. Roeske, and L. W. Snee. 1996. "The border ranges fault system in Glacier Bay National Park, Alaska: Evidence for major early Cenozoic dextral strike-slip motion." *Can. J. Earth Sci.* 33 (9): 1268–1282. https://doi.org/10.1139/e96-096.
Snieder, R., and E. Safak. 2006. "Extracting the building response using seismic interferometry: Theory and application to the Millikan library in Pasadena, California." *Bull. Seism. Soc. Am.* 96 (2): 586–598. https://doi.org/10.1785/0120050109.
Snieder, R., J. Sheiman, and R. Calvert. 2006. "Equivalence of the virtual-source method and wave-field deconvolution in seismic interferometry." *Phys. Rev. E* 73 (6): 066620. https://doi.org/10.1103/PhysRevE.73.066620.
Stein, R. S., J. R. Patton, and V. Sevilgen. 2018. "Exotic M=7.0 earthquake strikes beneath Anchorage, Alaska." Accessed August 15, 2019. http://temblor.net/earthquake-insights/exotic-m7-0-earthquake-strikes-beneath-anchorage-alaska-8010/.
Thornley, J., U. Dutta, P. Fahringer, and Z. Yang. 2019. "In situ shear-wave velocity measurements at the Delaney Park Downhole Array, Anchorage, Alaska." *Seismol. Res. Lett.* 90 (1): 395–400. https://doi.org/10.1785/0220180178.
Tikhonov, A. N., and V. Y. Arsenin. 1977. *Solution of ill-posed problems*. Washington, DC: Winston/Wiley.
Trampert, J., M. Cara, and M. Frogneux. 1993. "SH propagator matrix and QS estimates from borehole- and surface-recorded earthquake data." *Geophys. J. Int.* 112 (2): 290–299. https://doi.org/10.1111/j.1365-246X.1993.tb01456.x.
Ulery, C. A., and R. G. Updike. 1983. *Subsurface structure of the cohesive facies of the Bootlegger Cove formation, southwest Anchorage: Alaska*. Fairbanks, AK: Division of Geological & Geophysical Surveys.
Updike, R. G., and B. A. Carpenter. 1986. *Engineering geology of the Government Hill area, Anchorage, Alaska (No. 1588)*. Washington, DC: Dept. of the Interior, USGS.
USGS. 2018. "Earthquake hazards program." Accessed November 30, 2018. https://earthquake.usgs.gov/earthquakes/eventpage/ak20419010/executive.
Wen, W., and E. Kalkan. 2017. "System identification based on deconvolution and cross correlation: An application to a 20-story instrumented building in Anchorage, Alaska." *Bull. Seismol. Soc. Am.* 107 (2): 718–740.
Wen, W., and E. Kalkan. 2020. "Analyses of seismic waves at Delaney Park downhole array in Anchorage, Alaska." *Soil Dyn. Earthquake Eng.*
Wong, I., T. Dawson, M. Dober, and Y. Hashash. 2010. "Evaluating the seismic hazard in Anchorage, Alaska." In *Proc., 9th US National and 10th Canadian Conf. on Earthquake Engineering, Paper 785*. Oakland, CA: Earthquake Engineering Research Institute.
Yang, Z., U. Dutta, M. Çelebi, H. Liu, N. Biswas, T. Kono, and H. Benz. 2004. "Strong motion instrumentation and structural response of Atwood Building in downtown Anchorage, Alaska." In *Proc., 13th World Conf. on Earthquake Engineering*. Tokyo: International Association for Earthquake Engineering.
Yang, Z., U. Dutta, F. Xiong, N. Biswas, and H. Benz. 2008. "Seasonal frost effects on the dynamic behavior of a twenty-story office building." *Cold Reg. Sci. Technol.* 51 (1): 76–84. https://doi.org/10.1016/j.coldregions.2007.05.001.
Zerva, A. 2009. *Spatial variation of seismic ground motions: Modeling and engineering applications*. London: CRC Press.

Downloaded from ascelibrary.org by Harbin Institute of Technology on 10/24/20. Copyright ASCE. For personal use only; all rights reserved.